The Detection of Hot Molecular Cores in the Small Magellanic Cloud

Takashi Shimonishi[1] , Kei E. I. Tanaka[2,3,4] , Yichen Zhang[5,6] , and Kenji Furuya[4]

[1] Institute of Science and Technology, Niigata University, Ikarashi-nihoncho 8050, Nishi-ku, Niigata 950-2181, Japan; shimonishi@env.sc.niigata-u.ac.jp
[2] Department of Earth and Planetary Sciences, Tokyo Institute of Technology, Meguro, Tokyo, 152-8551, Japan
[3] Center for Astrophysics and Space Astronomy, University of Colorado Boulder, Boulder, CO 80309, USA
[4] National Astronomical Observatory of Japan, Osawa 2-21-1, Mitaka, Tokyo 181-8588, Japan
[5] Department of Astronomy, University of Virginia, Charlottesville, VA 22904-4325, USA
[6] Star and Planet Formation Laboratory, RIKEN Cluster for Pioneering Research, Wako, Saitama 351-0198, Japan
Received 2022 December 27; revised 2023 February 28; accepted 2023 March 1; published 2023 April 4

Abstract

We report the first detection of hot molecular cores in the Small Magellanic Cloud (SMC), a nearby dwarf galaxy with 0.2 solar metallicity. We observed two high-mass young stellar objects in the SMC with the Atacama Large Millimeter/submillimeter Array and detected emission lines of CO, HCO^+, $H^{13}CO^+$, SiO, H_2CO, CH_3OH, SO, and SO_2. Compact hot-core regions are traced by SO_2, whose spatial extent is about 0.1 pc, and the gas temperature is higher than 100 K based on the rotation diagram analysis. In contrast, CH_3OH, a classical hot-core tracer, is dominated by extended ($\sim$0.2–0.3 pc) components in both sources, and the gas temperature is estimated to be 39^{+8}_{-6} K for one source. Protostellar outflows are also detected from both sources as high-velocity components of CO. The metallicity-scaled abundances of SO_2 in hot cores are comparable among the SMC, Large Magellanic Cloud (LMC), and Galactic sources, suggesting that the chemical reactions leading to SO_2 formation would be regulated by elemental abundances. On the other hand, CH_3OH shows a large abundance variation within SMC and LMC hot cores. The diversity in the initial condition of star formation (e.g., degree of shielding, local radiation field strength) may lead to the large abundance variation of organic molecules in hot cores. This work, in conjunction with previous hot-core studies in the LMC and outer/inner Galaxy, suggests that the formation of a hot core would be a common phenomenon during high-mass star formation across the metallicity range of 0.2–1 $Z_\odot$. High-excitation SO_2 lines will be a useful hot-core tracer in the low-metallicity environments of the SMC and LMC.

Unified Astronomy Thesaurus concepts: Astrochemistry (75); Interstellar molecules (849); Protostars (1302); Magellanic Clouds (990); Complex organic molecules (2256); Radio astronomy (1338); Stellar jets (1607); Small Magellanic Cloud (1468); Metallicity (1031)

1. Introduction

Hot molecular cores are compact ($\lesssim$0.1 pc), dense ($\gtrsim$10^6 cm^{-3}), and hot ($\gtrsim$100 K) protostellar sources that appear in the early evolutionary stage of massive star formation (e.g., Kurtz et al. 2000). By the observations of Galactic star-forming regions, a variety of molecular species, including complex organic molecules (COMs), are often detected in hot cores owing to their chemically rich nature (e.g., Herbst & van Dishoeck 2009). Obtaining a comprehensive view of chemical compositions of hot cores at various metallicities should help understand the effect of the metallicity on the chemical evolution of protostellar sources. Such studies are also important for understanding the physical and chemical processes of the interstellar medium (ISM) during star/planet formation in primordial galaxies.

The characteristic chemistry of a hot core is triggered by radiation from the protostar, which warms up the inner envelope and sublimate ice mantles formed in the earlier, colder evolutionary stage. Across the ice-sublimation radius, there is a sharp change in molecular abundances between the inner hot-core region ($\gtrsim$100 K) and the outer envelope ($\lesssim$100 K) (e.g., Charnley et al. 1992; Nomura & Millar 2004; Garrod et al. 2008). In lower-metallicity cores, if the grain size distribution is the same, the relative importance of solid-phase chemistry to gas-phase chemistry would be smaller because of the reduced total grain surface area and higher dust temperature. Thus, at lower metallicity, we naively expect that hot-core regions (i.e., regions where chemistry is dominated by ice sublimation in the vicinity of protostars) would become less distinguished from outer envelopes. The validity of such a simplified picture, however, should be examined carefully since many physical and chemical factors contribute to the observed features of hot cores.

With the advent of the Atacama Large Millimeter/submillimeter Array (ALMA), hot cores are now detected in low-metallicity environments of the Large Magellanic Cloud (LMC; $\sim$1/2–1/3 $Z_\odot$) (Shimonishi et al. 2016a, 2020; Sewiło et al. 2018, 2022a, 2022b) and the extreme outer Galaxy ($\sim$1/4 $Z_\odot$) (Shimonishi et al. 2021). Among LMC hot cores, the abundance of CH_3OH, one of the simplest COMs and a classical hot-core tracer, shows a large scatter: it is roughly a metallicity-scaled abundance of Galactic counterparts in some sources, while it is significantly depleted beyond the level of metallicity difference in other sources. In contrast, sulfur-bearing molecules, SO and SO_2, are commonly detected in LMC hot cores with similar abundances. However, the number of low-metallicity hot-core samples is currently still limited, and observational efforts to extend hot-core studies to even lower-metallicity environments are highly required.

The Small Magellanic Cloud (SMC) is a nearby star-forming dwarf galaxy located at a distance of 62.1 ± 1.9 kpc (Graczyk et al. 2014). The SMC harbors the lowest-metallicity

environment ($\sim$1/4–1/10 $Z_\odot$; e.g., Hunter et al. 2005; Choudhury et al. 2018) among the Local-Group star-forming galaxies where we can detect and spatially resolve dense gas tracers. It thus provides a valuable opportunity to study chemical processing triggered by star formation in a metal-poor environment. However, although the detection of several large molecules such as CH_3OH and SO_2 are reported for a cold molecular cloud core in the SMC (Shimonishi et al. 2018), a hot core is yet to be detected due to the lack of a systematic survey.

In this work, we report the first detection of hot molecular cores in the SMC based on observations with ALMA.

2. Targets, Observations, and Data Reduction

2.1. Targets

The present targets, S07 and S09 from our our survey catalog (see Section 2.2) (also known as 2MASS J00540342-7319384 and 2MASS J00445643-7310109, respectively) are classified as high-mass young stellar objects (YSOs) based on their infrared spectral characteristics (van Loon et al. 2010). Their bolometric luminosities are estimated to be $2.8 \times 10^4 \, L_\odot$ for S07 and $6.1 \times 10^4 \, L_\odot$ for S09, respectively (Oliveira et al. 2013). The absorption bands of silicate dust, H_2O ice, and CO_2 ice are detected in both sources, suggesting that they are still embedded in a dense core (Oliveira et al. 2013). The location of the sources within the SMC is shown in Appendix A.

2.2. Observations

Observations were made with ALMA in 2019 and 2022 as a Cycle 7 program (2019.1.01770.S, PI: K. Tanaka), which is a part of the "Magellanic Clouds Outflow and Chemistry Survey (MAGOS)" project, in which we observed ten sources in the SMC and 30 sources in the LMC. We also use the ALMA archival data, 2019.1.00534.S (PI: S. Zahorecz). The sky frequencies of 337.81–338.74, 343.59–344.95, 345.01–347.82, 350.44–352.10, and 356.15–359.80 GHz are covered by nine spectral windows in total with a velocity resolution of 0.40–0.43 km s^{-1}. Details of the observation settings are summarized in Appendix A.

2.3. Data Reduction

Raw data are processed with the Common Astronomy Software Applications (CASA) package (versions 5.6.1 and 6.2.1). The original synthesized beam size is $0\overset{''}{.}37$–$0\overset{''}{.}43 \times 0\overset{''}{.}30$–$0\overset{''}{.}33$ with the Briggs weighting and a robustness parameter of 0.5. For the spectral analysis in this work, all the images are convolved to have a common circular beam size of $0\overset{''}{.}43$, which corresponds to 0.13 pc at the distance of the SMC. The CASA task tclean is used for imaging, and the masking is done using the auto-multithresh algorithm. The synthesized images are corrected for the primary beam pattern using the impbcor task in CASA. The continuum image is constructed by selecting line-free channels. Before the spectral extraction, the continuum emission is subtracted from the spectral data using the uvcontsub task in CASA.

The spectra and continuum flux are extracted from the $0\overset{''}{.}43$ diameter circular region centered at R.A. $= 0^h54^m3\overset{s}{.}443$ and decl. $= -73°19'38\overset{''}{.}51$ (International Celestial Reference System, ICRS) for S07 and R.A. $= 0^h44^m56\overset{s}{.}421$ and decl. $= -73°10'11\overset{''}{.}20$ (ICRS) for S09, respectively. These positions correspond to the continuum and molecular line peaks of the sources.

3. Results and Analysis

3.1. Spectra

We identify spectral lines with the aid of the Cologne Database for Molecular Spectroscopy[7] (CDMS; Müller et al. 2001, 2005) and the molecular database of the Jet Propulsion Laboratory[8] (Pickett et al. 1998). Extracted spectra are shown in Appendix B.1. The detection criterion adopted here is 3σ significance level and the velocity coincidence with systemic velocities of S07 (163.1 km s^{-1}) and S09 (132.0 km s^{-1}), which are measured using the $SO(N_J = 8_9$–$7_8)$ line. For weak lines, two or three channels are binned to increase the sensitivity.

Molecular emission lines of CO, HCO^+, $H^{13}CO^+$, SiO, H_2CO, CH_3OH, SO, and SO_2 are detected in both S07 and S09. For SO_2 and CH_3OH, multiple high-excitation lines with different upper-state energies are detected. Line parameters are measured by fitting a Gaussian. We estimate the peak brightness temperature, the FWHM, the LSR velocity, and the integrated intensity for each line based on the fitting as summarized in Appendix B.2.

3.2. Images

Figure 1 shows synthesized images of continuum and molecular emission lines. The images are constructed by integrating spectral data in the velocity range where the emission is detected. For SO_2 and CH_3OH, several emission lines with similar upper-state energies are stacked to reduce the noise level. Most of the detected molecular emission lines have their intensity peak near the submillimeter continuum center, which also corresponds to the infrared peak of the sources. SiO emission is not shown in the figure since the line is weak, but it also shows a compact distribution at the continuum peak. We estimate the size of emission regions by fitting a two-dimensional Gaussian (see Table 1). We also estimated the deconvolved source sizes as $\sqrt{FWHM_{maj} \times FWHM_{min} - \Theta_{beam}^2}$, where $FWHM_{maj/min}$ is the major/minor FWHM size as estimated from the two-dimensional Gaussian fit, and Θ_{beam}^2 is the geometric mean of the beam major and minor axes. Note that only upper limits are estimated for the emission whose size is comparable with or smaller than the beam size. Details of the continuum and molecular line distributions are discussed in Section 4.1.

3.3. Column Densities and Gas Temperatures

We use the rotation diagram method to estimate column densities and temperatures of SO_2 in both sources and CH_3OH in S07 (Figure 2), while the number of detected CH_3OH lines in S09 is not sufficient for this purpose. The details of the formulae are described in Appendix C.1. For SO_2 in S09, a straight-line fit is separated into low- and high-temperature regimes ($E_u < 60$ K and $E_u > 60$ K) because different temperature components are clearly seen in the diagram. The high-temperature components of SO_2 with $T_{rot} > 100$ K are detected in both sources. Derived parameters are summarized in Table 1.
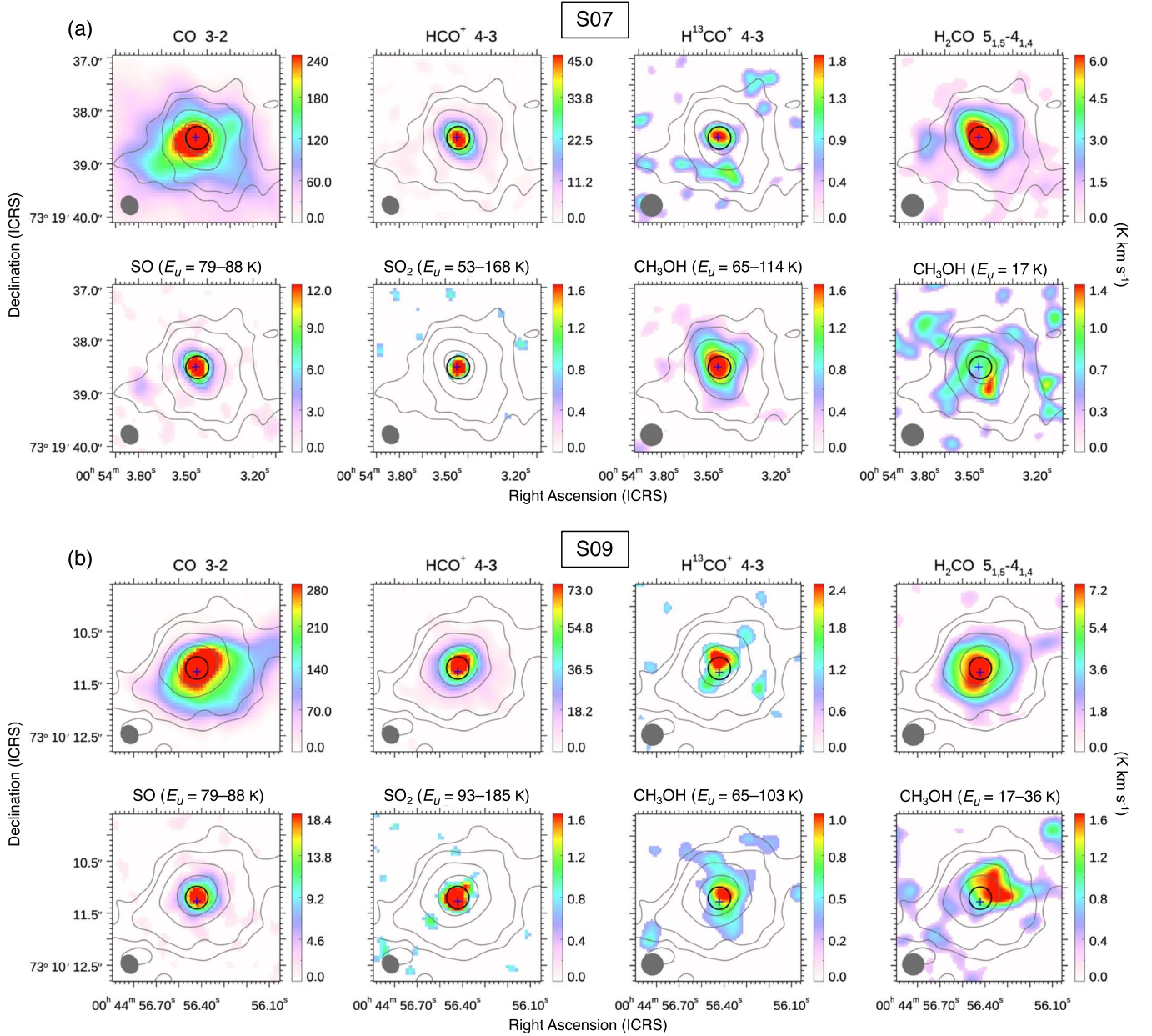

Figure 1. Integrated intensity distributions of molecular emission lines. Gray contours represent the 850 μm continuum distribution, and the contour levels are 3σ, 6σ, 15σ, and 40σ of the rms noise (0.03–0.04 mJy beam^{-1}). Low signal-to-noise ratio regions (S/N<1.5) are masked. The spectra discussed in the text are extracted from the region indicated by the black open circle. The blue cross represents the infrared peak position. The synthesized beam size is shown by the gray filled circle in each panel. North is up, and east is to the left.

For other molecules, the rotation temperatures are assumed for the column density estimation. We have applied low rotation temperatures from 30 to 60 K because the analyses for hot cores in the LMC and the outer Galaxy report $T_{\rm rot} \sim 40$–50 K for relatively small molecules with extended spatial distributions, such as SO and CS (Shimonishi et al. 2020, 2021). The same temperature range is applied for CH$_3$OH in S09, which also shows an extended distribution. If the rotation temperature of CH$_3$OH in S09 is assumed to be the same as that of the high-temperature component of SO$_2$, then we obtain a twice higher CH$_3$OH column density.

3.4. H$_2$ Column Density and Abundances

The column density of molecular hydrogen ($N_{\rm H_2}$) is estimated from the dust continuum data based on the standard treatment of optically thin emission (see Appendix C.2 for details). The assumption of the dust temperature T_d may cause considerable uncertainty in the derivation of $N_{\rm H_2}$. A detailed analysis of effective dust temperature in the line of sight toward an LMC hot core suggests that T_d is somewhat lower than the temperature of a hot-core region traced by SO$_2$ or CH$_3$OH due to the temperature gradient in a protostellar envelope (Shimonishi et al. 2020). In this work, we have applied T_d from 50 to 100 K to estimate the possible range of the $N_{\rm H_2}$ values. The 850 μm continuum brightness is measured to be 1.52 mJy beam^{-1} for S07 and 2.62 mJy beam^{-1} for S09 (with a beam size of $0\rlap{.}''37 \times 0\rlap{.}''32$), and with the above assumption, we obtain $N_{\rm H_2} = (1.5 \pm 0.5) \times 10^{23}$ cm^{-2} for S07 and $(2.5 \pm 0.8) \times 10^{23}$ cm^{-2} for S09, respectively. Fractional molecular abundances with respect to H$_2$ are calculated using
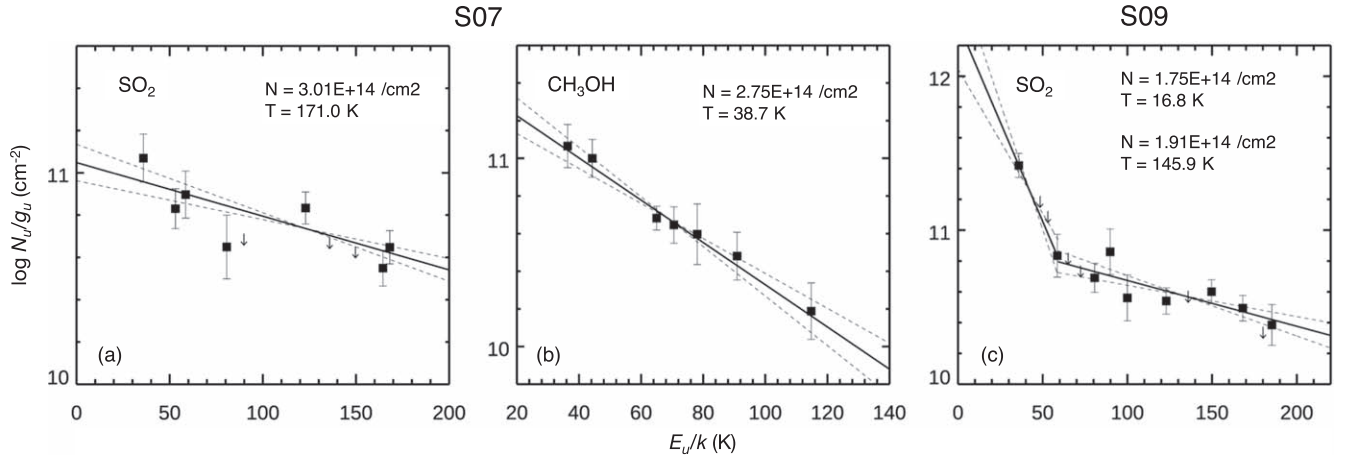
Figure 2. Results of rotation diagram analyses. Upper limit points are indicated by the down arrows. The solid lines represent the fitted straight line, while the dashed lines indicate the acceptable fits within 2σ level. Derived column densities and rotation temperatures are shown in each panel. See Section 3.3 for details.

Table 1
Estimated Rotation Temperatures, Column Densities, and Source Sizes

Object / Molecule	$T_{\rm rot}$ (K)	$N(X)$ (cm^{-2})	$N(X)/N_{\rm H_2}$	Size[a] ($''$/pc)	Size$_{\rm deconv}$[b] ($''$/pc)	Note
S07						
H$_2$	⋯	$(1.5 \pm 0.5) \times 10^{23}$	⋯	0.65/0.20[c]	0.55/0.17[c]	(1)
SO$_2$	171^{+65}_{-37}	$(3.0^{+0.7}_{-0.5}) \times 10^{14}$	$(2.0 \pm 0.8) \times 10^{-9}$	0.32/0.10	$\lesssim$0.17/0.05[d]	(2)
CH$_3$OH	39^{+8}_{-6}	$(2.8^{+1.0}_{-0.7}) \times 10^{14}$	$(1.8 \pm 0.9) \times 10^{-9}$	0.82/0.25[e]	0.70/0.21[e]	(2)
SO	30–60	$(3.5 \pm 1.4) \times 10^{14}$	$(2.3 \pm 1.0) \times 10^{-9}$	0.48/0.15	0.32/0.10	(3)
SiO	30–60	$(3.1 \pm 0.9) \times 10^{12}$	$(2.1 \pm 0.9) \times 10^{-11}$	⋯	⋯	(3)
H$_2$CO	30–60	$(3.6 \pm 0.1) \times 10^{13}$	$(2.4 \pm 0.8) \times 10^{-10}$	0.89/0.27	0.78/0.24	(3)
HCO$^+$	30–60	$(2.0 \pm 0.1) \times 10^{13}$	$(1.3 \pm 0.4) \times 10^{-10}$	0.55/0.17	0.26/0.08	(3)
HCO$^+$ (^{13}C)	⋯	$(5.5 \pm 1.7) \times 10^{13}$	$(3.7 \pm 1.1) \times 10^{-10}$	⋯	⋯	(4)
H^{13}CO$^+$	30–60	$(1.1 \pm 0.1) \times 10^{12}$	$(7.3 \pm 2.5) \times 10^{-12}$	0.44/0.13	$\lesssim$0.22/0.07[d]	(3)
CO	30–60	$>2 \times 10^{17}$	$>1 \times 10^{-6}$	1.27/0.38	1.22/0.37	(5)
S09						
H$_2$	⋯	$(2.5 \pm 1.0) \times 10^{23}$	⋯	0.68/0.21[c]	0.58/0.18[c]	(1)
SO$_2$ ($E_u > 80$ K)	146^{+68}_{-35}	$(1.9^{+0.7}_{-0.5}) \times 10^{14}$	$(7.2 \pm 5.9) \times 10^{-10}$	0.46/0.14	0.30/0.09	(6)
SO$_2$ ($E_u < 60$ K)	17^{+6}_{-4}	$(1.8^{+1.7}_{-0.9}) \times 10^{14}$	$(7.6 \pm 3.9) \times 10^{-10}$	⋯	⋯	(6)
CH$_3$OH	30–60	$(1.6 \pm 0.5) \times 10^{14}$	$(6.4 \pm 3.2) \times 10^{-10}$	0.93/0.28[e]	0.82/0.25[e]	(7)
SO	30–60	$(3.5 \pm 1.1) \times 10^{14}$	$(1.4 \pm 0.7) \times 10^{-9}$	0.58/0.18	0.46/0.14	(3)
SiO	30–60	$<2 \times 10^{12}$	$<8 \times 10^{-12}$	⋯	⋯	(3)
H$_2$CO	30–60	$(3.4 \pm 0.1) \times 10^{13}$	$(1.4 \pm 0.5) \times 10^{-10}$	1.06/0.32	0.97/0.30	(3)
HCO$^+$	30–60	$(2.9 \pm 0.1) \times 10^{13}$	$(1.2 \pm 0.5) \times 10^{-10}$	0.69/0.21	0.60/0.18	(3)
HCO$^+$ (^{13}C)	⋯	$(5.3 \pm 1.6) \times 10^{13}$	$(2.2 \pm 0.7) \times 10^{-10}$	⋯	⋯	(4)
H^{13}CO$^+$	30–60	$(1.1 \pm 0.1) \times 10^{12}$	$(4.4 \pm 1.9) \times 10^{-12}$	0.57/0.17	0.38/0.11	(3)
CO	30–60	$>2 \times 10^{17}$	$>8 \times 10^{-7}$	1.25/0.38	1.20/0.36	(5)

Notes. Uncertainties and upper limits are of 2σ level and do not include systematic errors due to adopted spectroscopic constants. (1) Based on dust continuum. T_d is varied from 50 to 100 K to estimate the range of possible $N_{\rm H_2}$. (2) Based on the rotation diagram. (3) $T_{\rm rot}$ is varied from 30 to 60 K to estimate the range of possible N(X). (4) Estimated from H^{13}CO$^+$ assuming ^{12}C/^{13}C = 50 (Heikkilä et al. 1999). An empirical 30% uncertainty is assumed. (5) Only lower limits since the line is optically thick. (6) Based on the rotation diagram analysis with two temperature components ($E_u > 80$ K and $E_u < 60$ K). (7) Estimated using CH$_3$OH(7_{-1} E–6_{-1} E).
[a] Source sizes estimated from a two-dimensional Gaussian fit to the emission peak (geometric mean of major and minor FWHM sizes).
[b] Deconvolved source size. Major and minor beam sizes range from $0''.43$–$0''.37$ and $0''.43$–$0''.32$. See Section 3.2 for details.
[c] Size of dust continuum emission.
[d] We set a minimum deconvolved size to be half the beam size to avoid unrealistically small source sizes.
[e] Size of high-E_u lines. Low-E_u lines are more extended.

those $N_{\rm H_2}$ and summarized in Table 1. The gas number density is estimated to be $n_{\rm H_2} = 6 \times 10^5$ cm^{-3} for S07 and 9×10^5 cm^{-3} for S09, assuming the source diameter of 0.13 pc and the uniform spherical distribution of gas around a protostar.

4. Discussion

4.1. Hot Molecular Cores Associated with S07 and S09

S07 and S09 show the following characteristics: (i) compact distribution of dense gas tracers ($\sim$0.1 pc; Section 3.2), (ii) high
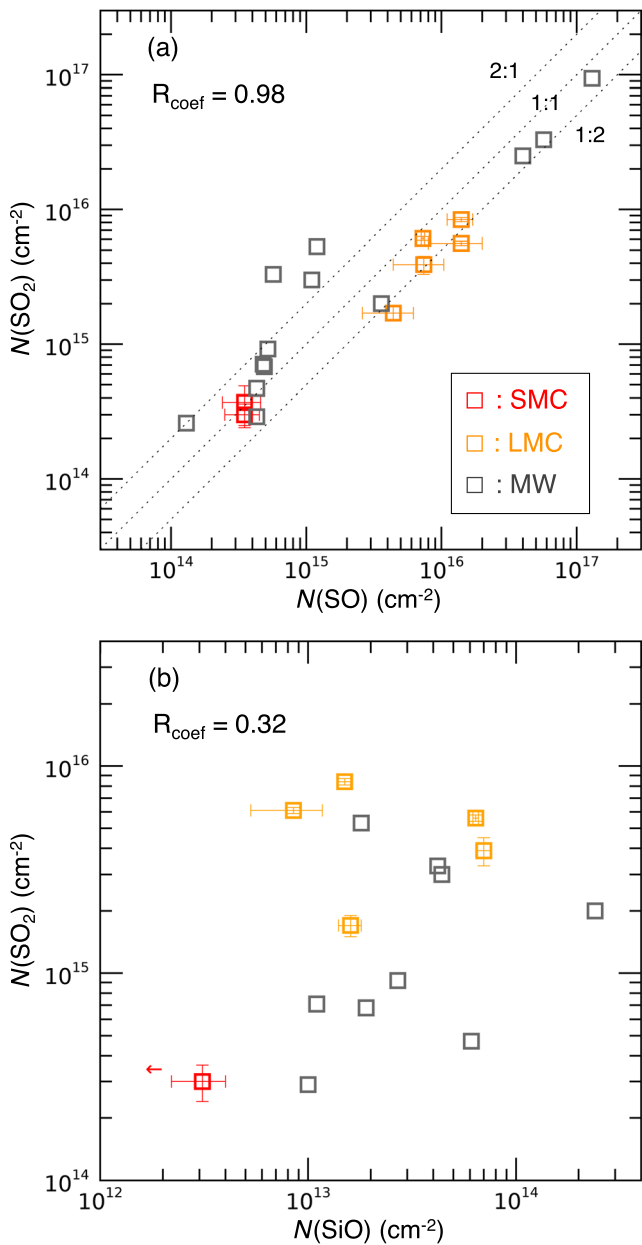
Figure 3. SO_2 column densities plotted against those of SO (a) and SiO (b) for SMC (red), LMC (orange), and Galactic (gray) hot cores. The dotted lines in panel (a) represent a ratio of 2:1, 1:1, and 1:2. The correlation coefficient (R_{coef}) is indicated.

gas temperature ($\geqslant$100 K; Section 3.3), (iii) high density ($\sim$10^6 cm^{-3}; Section 3.4), (iv) association with a high-mass protostar (3–$6 \times 10^4 \, L_\odot$), and (v) association with protostellar outflows (see Appendix D). These natures suggest that the sources are still in the early evolutionary stage of high-mass star formation, harboring a hot molecular core in the vicinity of the central protostar.

4.2. SO_2 as a Tracer of Low-metallicity Hot Cores

In both sources, a compact high-temperature region around the protostar is traced by SO_2 gas. The deconvolved source size of SO_2 is $\lesssim$0.05 pc for S07 and 0.09 pc for S09 (Table 1), which are comparable with or smaller than those of known LMC hot cores (Shimonishi et al. 2016b; Sewiło et al. 2018; Shimonishi et al. 2020; Sewiło et al. 2022b). With the local thermodynamic

equilibrium (LTE) assumption, the compact high-temperature regions in S07 and S09 are hot enough to sublimate the ice mantle, and the SO_2 gas likely arises mainly from the hot cores.

In contrast, the CH_3OH emission shows larger deconvolved source sizes (0.21 pc for S07 and 0.25 pc for S09) compared to that of SO_2 and associated with extended emission components. Although several high-E_u lines ($E_u > 60$ K) in S07 are detected, the rotation temperature is much lower than that of SO_2. Low-excitation CH_3OH lines ($E_u = 17$–36 K) are even extended, and the emission peak does not correspond to the hot-core position.

The clearly different spatial distributions and rotation temperatures between SO_2 and CH_3OH are in stark contrast to the characteristics of known LMC hot cores as their high-excitation SO_2 and CH_3OH lines are both compact ($\sim$0.1 pc) and hot ($T_{rot} > 100$ K) (e.g., Shimonishi et al. 2020; Sewiło et al. 2022b). In the present SMC hot cores, SO_2 and CH_3OH may have different physical origins.

Both SO_2 and CH_3OH are believed to be tracer molecules of hot cores in the Galactic and LMC star-forming regions. In hot cores, SO_2 could be formed by high-temperature gas-phase reactions of H_2S, HS, and OCS, which are sublimated from sulfur-bearing ices (e.g., Vidal & Wakelam 2018). If solid H_2S is a dominant sulfur reservoir in a prestellar stage, the expected major pathway to form SO_2 in a hot core is $H_2S \xrightarrow{H} SH \xrightarrow{H} S \xrightarrow{OH/O_2} SO \xrightarrow{OH} SO_2$, and the coevolution of SO and SO_2 abundances is predicted by astrochemical simulations (e.g., Charnley 1997; Nomura & Millar 2004). Alternatively, SO_2 can be produced at a prestellar stage by cosmic-ray-induced radiation chemistry and bulk reactions of reactive species in ice mantles (Shingledecker et al. 2020) and subsequently released into gas-phase by sublimation in a hot core.

Figure 3 compares the SO_2 column densities with those of SO and SiO for SMC, LMC, and Galactic hot cores (see Section 4.3 for the references of the plotted data). The SO_2 column densities show a tight correlation with SO (correlation coefficient: 0.98), while they do not correlate with the strong-shock tracer SiO (correlation coefficient: 0.32). This would suggest that the formation of SO_2 in the current sample is mainly induced by the sublimation of sulfur-bearing ices, rather than sputtering by strong shocks.

CH_3OH is reported to be efficiently formed by the successive hydrogenation of CO on grain surfaces (e.g., Watanabe & Kouchi 2002). The reaction typically proceeds at low temperatures ($\lesssim$20 K), and thus abundant solid CH_3OH can be formed in cold prestellar/protostellar stages (e.g., Boogert et al. 2011; Whittet et al. 2011). At the hot-core stage, the radiation from the protostar can trigger the thermal desorption of ice mantles, and if the abundant reservoir of solid CH_3OH is present, the abundance of gaseous CH_3OH will be significantly enhanced.

In the case of S07 and S09, such a high-temperature region is traced by hot SO_2 gas with a compact distribution centered at the continuum peak. A relatively low temperature and extended spatial distribution of CH_3OH suggest that the contribution from a nonthermal desorption is not negligible for its production in both sources. Considering the presence of protostellar outflows (Appendix D), sputtering of ice mantles by shock (e.g., Aota et al. 2015) or photodesorption by UV photons in an outflow cavity wall of the central protostar may be responsible for the desorption mechanism. Note that the latter mechanism is still under debate since laboratory experiments have reported that solid CH_3OH readily dissociates upon photodesorption by the UV irradiation (Bertin et al. 2016; Cruz-Diaz et al. 2016).
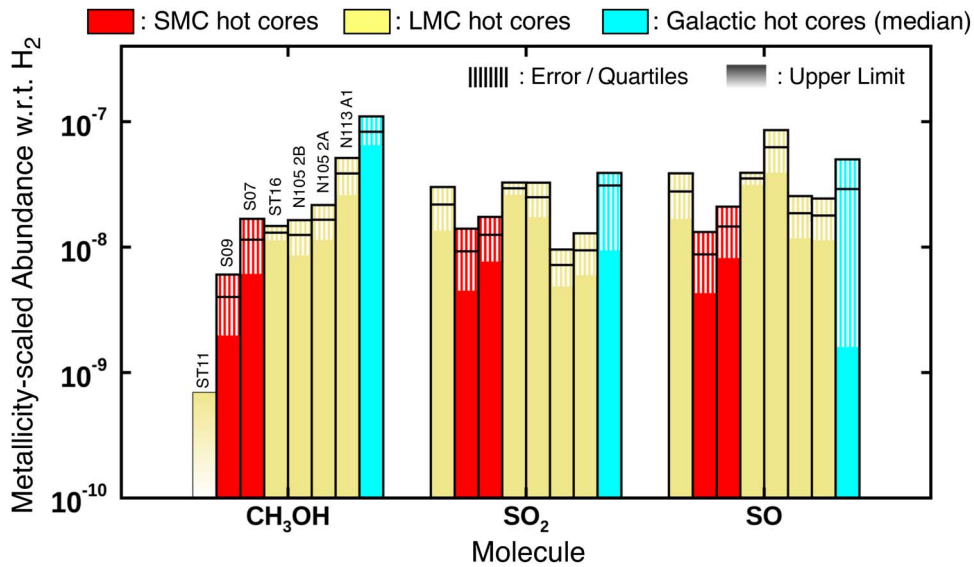
Figure 4. Comparison of metallicity-scaled molecular abundances of hot cores between SMC (red; this work), LMC (yellow), and Galactic sources (cyan). Abundances of SMC and LMC hot cores are multiplied by the corresponding metallicity factors (see Section 4.3). The area with thin vertical lines indicates the error bar for SMC/LMC sources, while those of Galactic sources indicate the lower and upper quartiles of the abundance distribution. The bar with a color gradient indicates an upper limit. See Section 4.3 for details.

4.3. Molecular Abundances

From the point of view of molecular abundances, SO_2 and CH_3OH show different source-to-source variations within LMC/ SMC hot cores. Figure 4 shows a comparison of metallicity-scaled molecular abundances for SMC, LMC, and Galactic hot cores. The data of LMC hot cores are adopted from Shimonishi et al. (2016a, 2020) and Sewiło et al. (2022b), where the N_{H_2} of ST11, N105 2B/2A, and N113 A1 are reestimated using the same dust opacity data as in this work and dust temperature of $T_d = 60$ K. Abundances for Galactic sources are collected from the literature for a sample of 11–17 hot cores (Sutton et al. 1995; MacDonald et al. 1996; Helmich & van Dishoeck 1997; Hatchell et al. 1998; van der Tak et al. 2000; Qin et al. 2010; Zernickel et al. 2012; Xu & Wang 2013; Gerner et al. 2014). In the figure, the lower and upper quartiles of the abundance distributions are plotted with the median value. HCO^+ abundances are calculated from $H^{13}CO^+$ assuming $^{12}C/^{13}C = 49$, 50, and 77 for SMC, LMC, and Galactic sources (Wilson & Rood 1994; Heikkilä et al. 1999; Wang et al. 2009).

In Figure 4, to correct for the metallicity difference, the molecular abundances of SMC and LMC hot cores are scaled in accordance with their metallicities. We have estimated the local metallicities of the individual hot cores based on the metallicity maps of the SMC and LMC reported in Choudhury et al. (2016, 2018). The metallicity for the two SMC hot cores is measured to be [Fe/H] = −0.8 dex (0.2 $Z_\odot$), while that for the LMC hot cores is typically [Fe/H] = −0.4 dex (0.4 $Z_\odot$). We assume a solar metallicity for Galactic hot cores.

As seen in the figure, the CH_3OH abundance shows large source-to-source variation even after corrected for the metallicity. In contrast, the metallicity-scaled abundance of SO_2 is relatively constant among SMC, LMC, and Galactic sources. The reason for the large abundance diversity of CH_3OH gas in LMC/SMC hot cores is still under debate. Astrochemical simulations for the chemical evolution of LMC/SMC hot cores suggest that dust temperature at the initial ice-forming stage has a significant effect on the CH_3OH gas abundance in the subsequent hot-core stage because the formation of solid CH_3OH is sensitive to dust temperature, and it is inhibited on warmer grain surfaces (Acharyya & Herbst 2018; Shimonishi et al. 2020). Therefore, the diversity in the initial condition of star formation (e.g., degree of shielding, local radiation field strength) may lead to the large abundance variation of CH_3OH. Infrared ice observations argue that the inhibition of solid CH_3OH in the ice-forming stage is more likely to occur in the LMC condition due to the lower dust abundance and the stronger interstellar radiation field (Shimonishi et al. 2016a).

On the other hand, SO_2 would not be inherited from the prestellar stage to the hot-core stage because it is mainly synthesized by high-temperature gas-phase chemistry. Thus, except for the elemental abundance effect, the local interstellar condition would not largely affect the SO_2 abundance in hot cores, which may result in a constant metallicity-scaled abundance of SO_2 across SMC, LMC, and Galactic sources. Such behavior of SO_2 is predicted by the astrochemical simulations dedicated to LMC hot cores (Shimonishi et al. 2020), but now the present study suggests that it is also applicable to SMC hot cores.

5. Summary

We report the detection of two hot molecular cores in the SMC based on 0.1 pc-scale submillimeter observations toward high-mass YSOs with ALMA. Emission lines of CO, HCO^+, $H^{13}CO^+$, SiO, H_2CO, CH_3OH, SO, and SO_2 are detected from the sources. The associated protostellar outflows are also observed. The compact hot-core regions are traced by SO_2 gas, whose spatial extent is about 0.1 pc, and the gas temperature is higher than 100 K based on the excitation analysis. In contrast, CH_3OH, a classical hot-core tracer, is dominated by extended (∼0.2–0.3 pc) components, and low gas temperature (<40 K) is inferred for one source. The metallicity-scaled abundances of SO_2 in hot cores are comparable between SMC, LMC, and Galactic sources, suggesting that the chemical reactions leading to the formation of SO_2 would be regulated by the sulfur abundances. On the other hand, CH_3OH shows a large abundance variation within SMC and LMC hot cores. This difference would be due to their different chemical origin. High-excitation SO_2 lines will be a useful tracer of hot cores

in the low-metallicity environments of the SMC and LMC. In conjunction with previous hot-core studies in the LMC and outer/inner Galaxy, the formation of a hot core would be a common phenomenon during star formation across the metallicity range of 0.2–1 $Z_\odot$.

This paper makes use of the following ALMA data: ADS/JAO.ALMA#2019.1.01770.S and 2019.1.00534.S. ALMA is a partnership of ESO (representing its member states), NSF (USA) and NINS (Japan), together with NRC (Canada), MOST and ASIAA (Taiwan), and KASI (Republic of Korea), in cooperation with the Republic of Chile. The Joint ALMA Observatory is operated by ESO, AUI/NRAO and NAOJ. This work has made extensive use of the Cologne Database for Molecular Spectroscopy and the molecular database of the Jet

Software: CASA (McMullin et al. 2007).

Appendix A
Observation Summary

Table A1 summarizes the details of the present ALMA Band 7 observations. The location of the present hot cores in the SMC is shown in Figure A1.

Table A1
Observation Summary

Object / Proposal ID	Observation Date	On-source Time (min)	Mean PWV[a] (mm)	Number of Antennas	Baseline[b]		Beam Size[c] ($'' \times ''$)	MRS[d] ($''$)	Channel Spacing (MHz)
					L5 (m)	L80 (m)			
S07									
2019.1.00534.S	2019 Oct 17–21	35.3	0.5–0.9	42–45	36.0	278.1	0.41 × 0.30	4.9	0.49
2019.1.00534.S	2019 Oct 6–7	22.7	0.5	39–44	44.5	351.2	0.39 × 0.32	4.0	0.49
2019.1.01770.S	2019 Oct 21–23, 2022 Jan 6, 2022 May 17	24.2	0.5–1.1	44–48	35.2	270.7	0.36 × 0.32	5.0	0.49
S09									
2019.1.00534.S	2019 Oct 17– 2019 Oct 21	36.3	0.5–0.9	42-45	36.1	277.9	0.41 × 0.30	4.8	0.49
2019.1.00534.S	2019 Oct 6– 2019 Oct 7	22.7	0.5	39–44	44.8	351.3	0.39 × 0.32	4.0	0.49
2019.1.01770.S	2019 Oct 21–23, 2022 Jan 6, 2022 May 17	24.2	0.5–1.1	44–48	35.4	271.7	0.36 × 0.32	5.0	0.49

Notes.
[a] Precipitable water vapor.
[b] L5/L80 indicate the length that includes the 5th/80th percentile of all projected baselines.
[c] The average beam size of aggregated continuum. Note that we use a common circular restoring beam size of 0.″43 for the spectral analysis.
[d] Maximum recoverable scale.
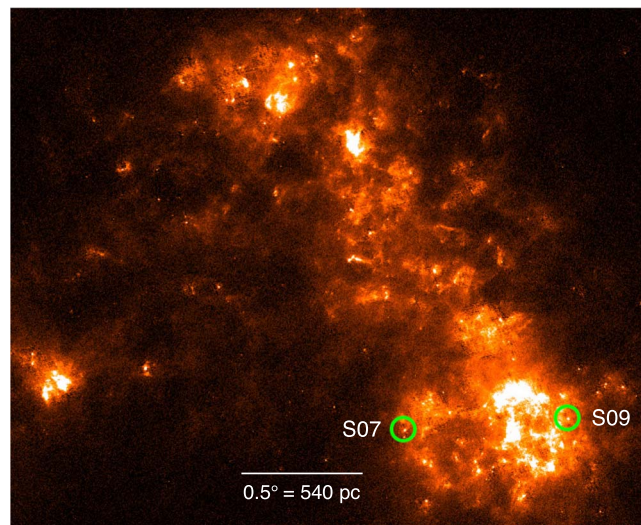
Figure A1. Location of the present hot cores, S07 and S09, within the SMC (the green solid circle). The background is a Herschel/PACS 160 μm image obtained by the HERITAGE program (Meixner et al. 2013). North is up, and east is to the left.

Appendix B
Fitted Spectra and Measured Line Parameters

B.1. Fitted Spectra

Figures B1–B2 show the results of the spectral line fitting (see Section 3.1 for details).
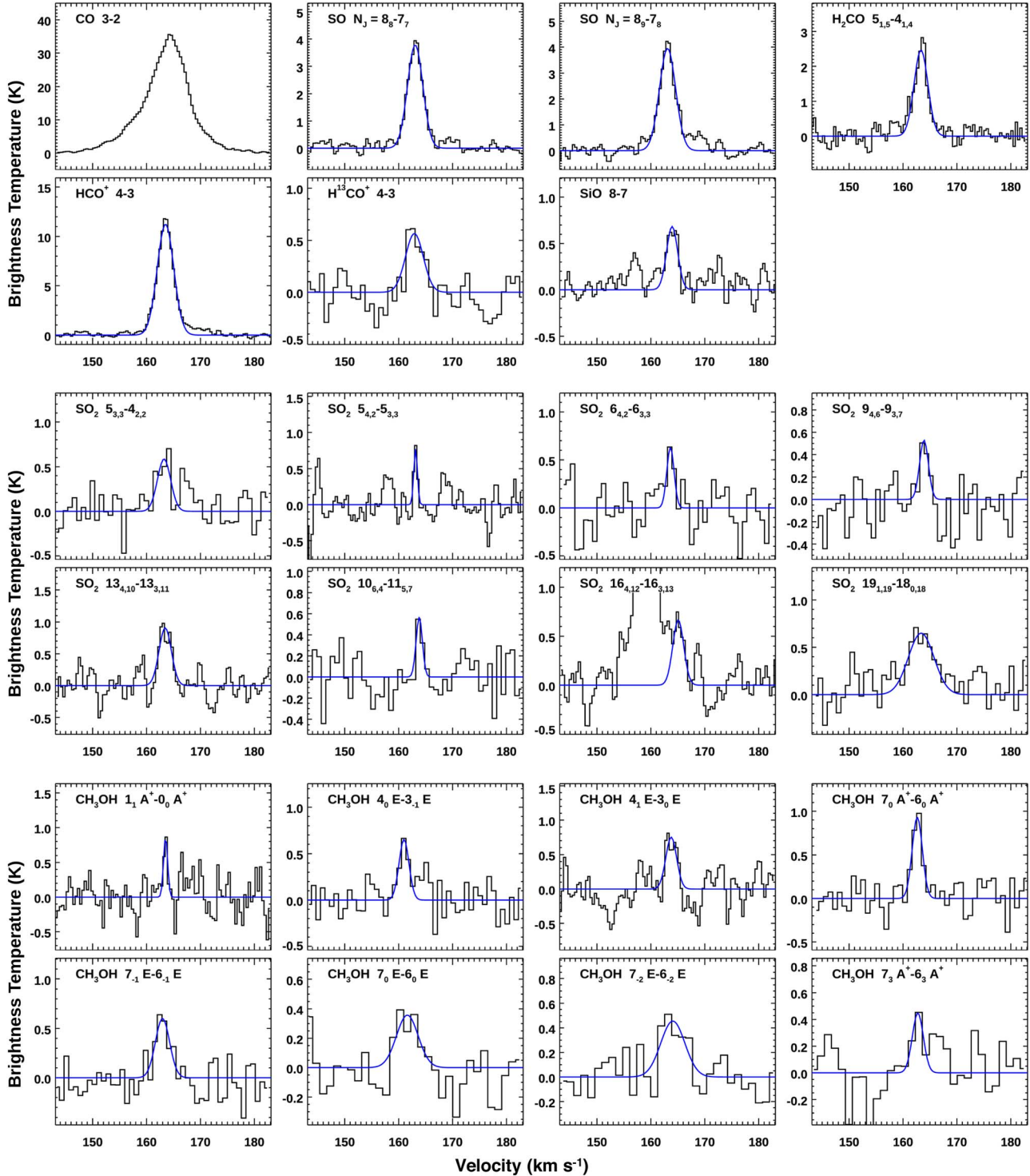
Figure B1. ALMA spectra of molecular emission lines detected in S07. The blue lines represent fitted Gaussian profiles. For SO$_2$ and CH$_3$OH, the spectra are sorted in ascending order of the upper-state energy (the emission line with the lowest upper-state energy is shown in the upper left panel and that with the highest energy is in the lower right panel). The adjacent stronger line seen in SO$_2$(16$_{4,12}$–16$_{3,13}$) was subtracted before fitting the main line.
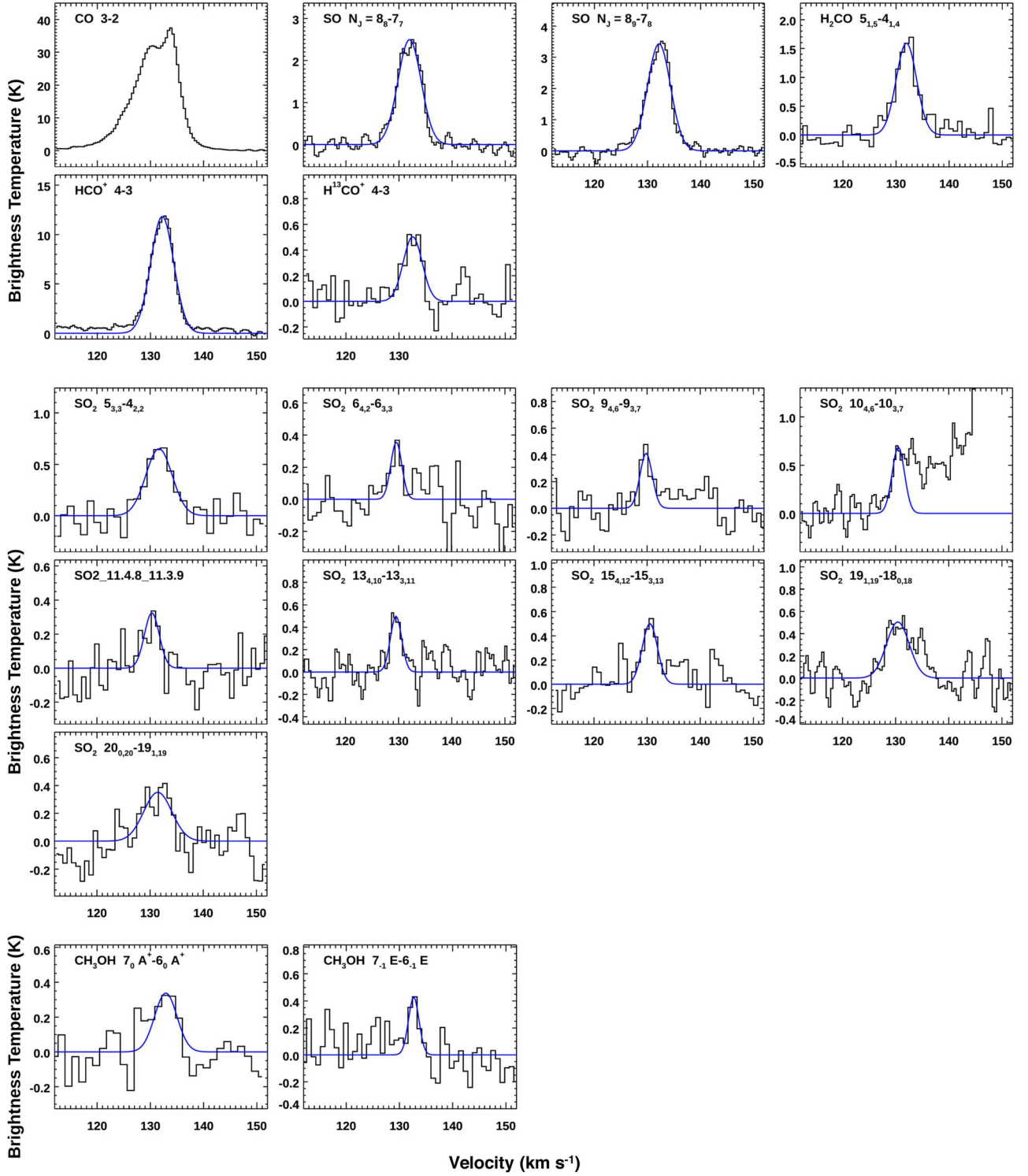
Figure B2. Same as in Figure B1 but for S09. The adjacent stronger line seen in $SO_2(10_{4,6}-10_{3,7})$ was subtracted before fitting the main line.

B.2. Measured Line Parameters

Tables B1–B2 summarize line parameters measured by spectral fitting (see Section 3.1 for details). T_{br}, ΔV, $\int T_{br}\, dV$, and V_{LSR} indicate the peak brightness temperature, the FWHM, the integrated intensity, and the systemic velocity. For CO(3–2), since it shows a clear non-Gaussian component, the integrated intensity is calculated by directly integrating the spectrum over the frequency region of emission. The tables also contain the upper limits on important nondetection lines. The tabulated uncertainties and upper limits are of 2σ level and do not include systematic errors due to continuum subtraction. Upper limits on integrated intensities are estimated assuming $\Delta V = 4$ km s^{-1}. Note that the systemic velocities of S07 and S09 mentioned in the text are based on the SO($N_J = 8_9-7_8$) line.

Table B1
Line Parameters of S07

Molecule	Transition	E_u (K)	Frequency (GHz)	T_{br} (K)	ΔV (km s^{-1})	$\int T_{br}\,dV$ (K km s^{-1})	V_{LSR} (km s^{-1})	rms (K)	Note
CO	3–2	33	345.79599	35.58 ± 0.39	∼10	336.3 ± 0.4	164.0	0.20	(1)
HCO$^+$	4–3	43	356.73422	11.25 ± 0.08	3.6	43.2 ± 0.7	163.5	0.24	⋯
H^{13}CO$^+$	4–3	42	346.99834	0.57 ± 0.05	3.9	2.3 ± 0.5	162.9	0.13	⋯
H$_2$CO	$5_{1,5}$–$4_{1,4}$	62	351.76864	2.46 ± 0.07	3.0	8.0 ± 0.5	163.3	0.24	⋯
SiO	8–7	75	347.33058	0.68 ± 0.05	2.4	1.8 ± 0.3	163.9	0.18	⋯
SO	$N_J = 8_8$–7_7	87	344.31061	3.78 ± 0.06	3.4	13.6 ± 0.5	163.1	0.20	⋯
SO	$N_J = 8_9$–7_8	79	346.52848	3.95 ± 0.05	3.6	14.9 ± 0.5	163.1	0.18	⋯
SO$_2$	$20_{1,19}$–$19_{2,18}$	199	338.61181	<0.30	⋯	<1.3	⋯	0.15	⋯
SO$_2$	$16_{4,12}$–$16_{3,13}$	164	346.52388	0.67 ± 0.05	2.4	1.7 ± 0.3	165.1	0.18	(2)
SO$_2$	$19_{1,19}$–$18_{0,18}$	168	346.65217	0.65 ± 0.05	5.6	3.9 ± 0.7	163.4	0.13	⋯
SO$_2$	$10_{6,4}$–$11_{5,7}$	139	350.86276	0.57 ± 0.07	1.4	0.8 ± 0.3	163.8	0.17	⋯
SO$_2$	$5_{3,3}$–$4_{2,2}$	36	351.25722	0.58 ± 0.06	2.9	1.8 ± 0.5	163.2	0.17	⋯
SO$_2$	$14_{4,10}$–$14_{3,11}$	136	351.87387	<0.48	⋯	<2.1	⋯	0.24	⋯
SO$_2$	$10_{4,6}$–$10_{3,7}$	90	356.75519	<0.34	⋯	<1.4	⋯	0.17	⋯
SO$_2$	$13_{4,10}$–$13_{3,11}$	123	357.16539	0.91 ± 0.06	2.7	2.6 ± 0.5	163.5	0.24	⋯
SO$_2$	$15_{4,12}$–$15_{3,13}$	150	357.24119	<0.48	⋯	<2.0	⋯	0.24	⋯
SO$_2$	$9_{4,6}$–$9_{3,7}$	81	357.67182	0.53 ± 0.07	1.9	1.1 ± 0.4	163.9	0.17	⋯
SO$_2$	$8_{4,4}$–$8_{3,5}$	72	357.58145	<0.50	⋯	<2.1	⋯	0.17	⋯
SO$_2$	$7_{4,4}$–$7_{3,5}$	65	357.89244	<0.34	⋯	<1.4	⋯	0.17	⋯
SO$_2$	$6_{4,2}$–$6_{3,3}$	59	357.92585	0.63 ± 0.06	1.6	1.1 ± 0.3	163.6	0.17	⋯
SO$_2$	$17_{4,14}$–$17_{3,15}$	180	357.96290	<0.34	⋯	<1.4	⋯	0.17	⋯
SO$_2$	$5_{4,2}$–$5_{3,3}$	53	358.01315	0.77 ± 0.08	0.8	0.7 ± 0.1	163.1	0.24	⋯
SO$_2$	$20_{0,20}$–$19_{1,19}$	185	358.21563	<0.39	⋯	<1.7	⋯	0.20	⋯
CH$_3$OH	7_0 E–6_0 E	78	338.12449	0.36 ± 0.06	4.8	1.8 ± 0.7	161.6	0.12	⋯
CH$_3$OH	7_{-1} E–6_{-1} E	71	338.34459	0.60 ± 0.06	3.1	2.0 ± 0.4	163.0	0.15	⋯
CH$_3$OH	7_0 A$^+$–6_0 A$^+$	65	338.40870	0.93 ± 0.06	2.2	2.2 ± 0.3	162.6	0.15	⋯
CH$_3$OH	7_2 A$^-$–6_2 A$^-$	103	338.51285	<0.24	⋯	<1.0	⋯	0.12	(3)
CH$_3$OH	7_3 A$^+$–6_3 A$^+$	115	338.54083	0.45 ± 0.06	2.4	1.2 ± 0.4	162.7	0.12	(4)
CH$_3$OH	7_{-3} E–6_{-3} E	128	338.55996	<0.24	⋯	<1.0	⋯	0.12	⋯
CH$_3$OH	7_3 E–6_3 E	113	338.58322	<0.24	⋯	<1.0	⋯	0.12	⋯
CH$_3$OH	7_1 E–6_1 E	86	338.61494	<0.50	⋯	<2.1	⋯	0.15	⋯
CH$_3$OH	7_2 A$^+$–6_2 A$^+$	103	338.63980	<0.24	⋯	<1.0	⋯	0.12	⋯
CH$_3$OH	7_{-2} E–6_{-2} E	91	338.72290	0.46 ± 0.06	5.3	2.6 ± 0.7	164.1	0.12	(4)
CH$_3$OH	5_4 A$^-$–6_3 A$^-$	115	346.20272	<0.26	⋯	<1.1	⋯	0.13	(4)
CH$_3$OH	4_0 E–3_{-1} E	36	350.68766	0.65 ± 0.07	2.2	1.5 ± 0.4	161.0	0.17	⋯
CH$_3$OH	1_1 A$^+$–0_0 A$^+$	17	350.90510	0.87 ± 0.09	0.9	0.8 ± 0.2	163.5	0.24	⋯
CH$_3$OH	4_1 E–3_0 E	44	358.60580	0.75 ± 0.07	2.4	1.9 ± 0.4	163.8	0.28	⋯

Note. (1) $\int T_{br}\,dV$ is calculated by directly integrating the spectrum from 145 km s^{-1} to 180 km s^{-1}. (2) Partial blend with SO($N_J = 8_9$–7_8). (3) Blend of three CH$_3$OH lines with similar spectroscopic constants. (4) Blend of two CH$_3$OH lines with similar spectroscopic constants.

Table B2
Line Parameters of S09

Molecule	Transition	E_u (K)	Frequency (GHz)	T_{br} (K)	ΔV (km s^{-1})	$\int T_{br}\,dV$ (K km s^{-1})	V_{LSR} (km s^{-1})	rms (K)	Note
CO	3–2	33	345.79599	37.40 ± 0.27	∼10	361.4 ± 0.3	131.3	0.13	(1)
HCO$^+$	4–3	43	356.73422	11.84 ± 0.05	5.1	64.47 ± 0.56	132.2	0.14	⋯
H^{13}CO$^+$	4–3	42	346.99834	0.50 ± 0.04	4.2	2.25 ± 0.37	132.6	0.09	⋯
H$_2$CO	$5_{1,5}$–$4_{1,4}$	62	351.76864	1.63 ± 0.06	4.4	7.66 ± 0.58	131.9	0.20	⋯
SiO	8–7	75	347.33058	<0.18	⋯	<0.8	⋯	0.09	⋯
SO	$N_J = 8_8$–7_7	87	344.31061	2.50 ± 0.04	5.2	13.70 ± 0.49	132.0	0.13	⋯
SO	$N_J = 8_9$–7_8	79	346.52848	3.43 ± 0.04	5.1	18.70 ± 0.49	132.2	0.13	⋯
SO$_2$	$20_{1,19}$–$19_{2,18}$	199	338.61181	<0.50	⋯	<2.1	⋯	0.12	⋯
SO$_2$	$16_{4,12}$–$16_{3,13}$	164	346.52388	<0.80	⋯	<3.4	⋯	0.13	(2)
SO$_2$	$19_{1,19}$–$18_{0,18}$	168	346.65217	0.51 ± 0.03	5.0	2.72 ± 0.52	130.4	0.13	⋯
SO$_2$	$10_{6,4}$–$11_{5,7}$	139	350.86276	<0.27	⋯	<1.4	⋯	0.14	⋯
SO$_2$	$5_{3,3}$–$4_{2,2}$	36	351.25722	0.65 ± 0.05	5.9	4.05 ± 0.73	131.7	0.11	⋯
SO$_2$	$14_{4,10}$–$14_{3,11}$	136	351.87387	<0.39	⋯	<1.7	⋯	0.20	⋯
SO$_2$	$10_{4,6}$–$10_{3,7}$	90	356.75519	0.69 ± 0.04	2.8	2.02 ± 0.68	130.51	0.15	(3)
SO$_2$	$13_{4,10}$–$13_{3,11}$	123	357.16539	0.50 ± 0.04	2.5	1.33 ± 0.26	129.5	0.14	⋯

Table B2
(Continued)

Molecule	Transition	E_u (K)	Frequency (GHz)	T_{br} (K)	ΔV (km s^{-1})	$\int T_{br}\,dV$ (K km s^{-1})	V_{LSR} (km s^{-1})	rms (K)	Note
SO$_2$	$15_{4,12}-15_{3,13}$	150	357.24119	0.50 ± 0.04	3.4	1.80 ± 0.32	130.5	0.10	...
SO$_2$	$11_{4,8}-11_{3,9}$	100	357.38758	0.33 ± 0.04	3.3	1.14 ± 0.39	130.3	0.10	...
SO$_2$	$9_{4,6}-9_{3,7}$	81	357.67182	0.41 ± 0.04	2.7	1.20 ± 0.26	129.8	0.10	...
SO$_2$	$8_{4,4}-8_{3,5}$	72	357.58145	<0.29	...	<1.2	...	0.14	...
SO$_2$	$7_{4,4}-7_{3,5}$	65	357.89244	<0.29	...	<1.2	...	0.14	...
SO$_2$	$6_{4,2}-6_{3,3}$	59	357.92585	0.36 ± 0.04	2.5	0.93 ± 0.29	129.6	0.10	...
SO$_2$	$17_{4,14}-17_{3,15}$	180	357.96290	<0.29	...	<1.2	...	0.14	...
SO$_2$	$5_{4,2}-5_{3,3}$	53	358.01315	<0.29	...	<1.2	...	0.14	...
SO$_2$	$4_{4,0}-4_{3,1}$	48	358.03789	<0.20	...	<0.9	...	0.10	...
SO$_2$	$20_{0,20}-19_{1,19}$	185	358.21563	0.35 ± 0.04	6.2	2.32 ± 0.70	131.4	0.12	...
CH$_3$OH	7_0 E-6_0 E	78	338.12449	<0.25	...	<1.3	...	0.12	...
CH$_3$OH	7_{-1} E-6_{-1} E	71	338.34459	0.43 ± 0.05	2.3	1.06 ± 0.31	132.7	0.12	...
CH$_3$OH	7_0 A$^+$$-6_0$ A$^+$	65	338.40870	0.34 ± 0.04	4.9	1.78 ± 0.60	132.9	0.10	...
CH$_3$OH	7_1 E-6_1 E	86	338.61494	<0.25	...	<1.3	...	0.12	...
CH$_3$OH	7_2 A$^+$$-6_2$ A$^+$	103	338.63980	<0.25	...	<1.3	...	0.12	...
CH$_3$OH	4_0 E-3_{-1} E	36	350.68766	<0.22	...	<0.9	...	0.11	...
CH$_3$OH	1_1 A$^+$$-0_0$ A$^+$	17	350.90510	<0.20	...	<0.9	...	0.10	...
CH$_3$OH	4_1 E-3_0 E	44	358.60580	<0.25	...	<1.0	...	0.12	...

Note. (1) $\int T_{br}\,dV$ is calculated by directly integrating the spectrum from 114 km s^{-1} to 145 km s^{-1}. (2) Partial blend with SO($N_J = 8_9-7_8$). (3) Partial blend with HCO$^+$(4–3).

Appendix C
Derivation of Column Densities and Temperatures

C.1. Rotation Diagram Analysis

We use the following formulae based on the standard treatment of the rotation diagram method (e.g., Sutton et al. 1995):

$$\log\left(\frac{N_u}{g_u}\right) = -\left(\frac{\log e}{T_{rot}}\right)\left(\frac{E_u}{k}\right) + \log\left(\frac{N}{Q(T_{rot})}\right), \qquad \text{(C1)}$$

where

$$\frac{N_u}{g_u} = \frac{3k \int T_b dV}{8\pi^3 \nu S \mu^2}, \qquad \text{(C2)}$$

and N_u is a column density of molecules in the upper energy level, g_u is the degeneracy of the upper level, k is the Boltzmann constant, $\int T_b\,dV$ is the integrated intensity estimated from the observations, ν is the transition frequency, S is the line strength, μ is the dipole moment, T_{rot} is the rotational temperature, E_u is the upper-state energy, N is the total column density, and $Q(T_{rot})$ is the partition function at T_{rot}. We assume an optically thin condition and the LTE. All the spectroscopic parameters required in the analysis are extracted from the CDMS database.

C.2. Derivation of the H$_2$ Column Density from the Dust Continuum

We use the following equation to calculate N_{H_2} based on the standard treatment of optically thin dust emission:

$$N_{H_2} = \frac{F_\nu/\Omega}{2\kappa_\nu B_\nu(T_d)Z\mu m_H}, \qquad \text{(C3)}$$

where F_ν/Ω is the continuum flux density per beam solid angle as estimated from the observations, and κ_ν is the mass absorption coefficient of dust grains coated by thin ice mantles taken from Ossenkopf & Henning (1994), and we use 1.94 cm^2 g^{-1} for 850 μm, T_d is the dust temperature, and $B_\nu(T_d)$ is the Planck function, Z is the dust-to-gas mass ratio, μ is the mean atomic mass per hydrogen (1.41, according to Cox 2000), and m_H is the hydrogen mass. We use the dust-to-gas mass ratio of 0.0016, which is obtained by scaling the Galactic value of 0.008 by the metallicity of the SMC. The assumed dust temperature is described in the main text.

Appendix D
Molecular Outflows Traced by CO

Protostellar molecular outflows are detected in S07 and S09 as high-velocity CO(3–2) components (Figure D1). The presence of shocked H$_2$ gas associated with the protostar is
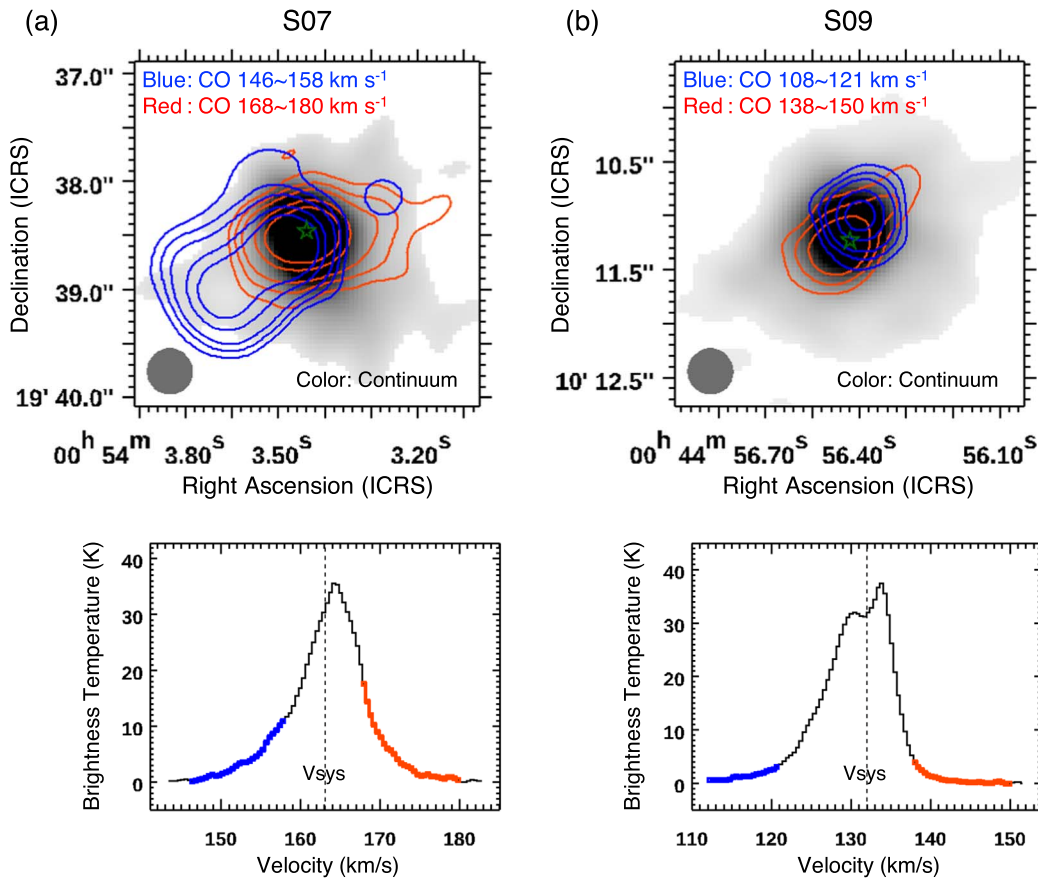
Figure D1. CO(3–2) outflows detected in S07 (a) and S09 (b). The upper panels show the spatial distribution of high-velocity CO gas. Blue contours represent the blueshifted component (integrated over 146–158 km s^{-1} for S07 and 108–121 km s^{-1} for S09), while red contours represent the redshifted component (integrated over 168–180 km s^{-1} for S07 and 138–150 km s^{-1} for S09). Background is the 850 μm continuum flux. The green stars represent the position of the protostar inferred from the continuum peak position. The synthesized beam size is shown by the gray filled circle in each panel. The lower panels show the CO(3–2) spectra extracted at the hot-core position as in Figures B1–B2. The velocity ranges of the blue- and redshifted high-velocity components are indicated by blue and red, respectively. The dotted lines indicate a systemic velocity of the source estimated from the SO($N_J = 8_8$–7_7) line.

reported in Ward et al. (2017) for both sources based on high-spatial resolution near-infrared integral field spectroscopy. The molecular component of outflows in S07 is recently reported by Tokuda et al. (2022) with ALMA observations of the CO(3–2) line. The outflows detected in S09 is the second example of CO-traced protostellar outflows found in the SMC. A detailed analysis of protostellar outflows for a sample of LMC/SMC YSOs will be reported in a future paper based on the MAGOS data (K. Tanaka et al. 2023, in preparation).

ORCID iDs

Takashi Shimonishi ● https://orcid.org/0000-0002-0095-3624
Kei E. I. Tanaka ● https://orcid.org/0000-0002-6907-0926
Yichen Zhang ● https://orcid.org/0000-0001-7511-0034
Kenji Furuya ● https://orcid.org/0000-0002-2026-8157

References

Acharyya, K., & Herbst, E. 2018, ApJ, 859, 51
Aota, T., Inoue, T., & Aikawa, Y. 2015, ApJ, 799, 141
Bertin, M., Romanzin, C., Doronin, M., et al. 2016, ApJL, 817, L12
Boogert, A. C. A., Huard, T. L., Cook, A. M., et al. 2011, ApJ, 729, 92
Charnley, S. B. 1997, ApJ, 481, 396
Charnley, S. B., Tielens, A. G. G. M., & Millar, T. J. 1992, ApJL, 399, L71
Choudhury, S., Subramaniam, A., & Cole, A. A. 2016, MNRAS, 455, 1855
Choudhury, S., Subramaniam, A., Cole, A. A., & Sohn, Y. J. 2018, MNRAS, 475, 4279

Cox, A. N. 2000, Allen's astrophysical quantities (Berlin: Springer)
Cruz-Diaz, G. A., Martín-Doménech, R., Muñoz Caro, G. M., & Chen, Y. J. 2016, A&A, 592, A68
Garrod, R. T., Weaver, S. L. W., & Herbst, E. 2008, ApJ, 682, 283
Gerner, T., Beuther, H., Semenov, D., et al. 2014, A&A, 563, A97
Graczyk, D., Pietrzyński, G., Thompson, I. B., et al. 2014, ApJ, 780, 59
Hatchell, J., Thompson, M. A., Millar, T. J., & MacDonald, G. H. 1998, A&A, 338, 713
Heikkilä, A., Johansson, L. E. B., & Olofsson, H. 1999, A&A, 344, 817
Helmich, F. P., & van Dishoeck, E. F. 1997, A&AS, 124, 205
Herbst, E., & van Dishoeck, E. F. 2009, ARA&A, 47, 427
Hunter, I., Dufton, P. L., Ryans, R. S. I., et al. 2005, A&A, 436, 687
Kurtz, S., Cesaroni, R., Churchwell, E., Hofner, P., & Walmsley, C. M. 2000, in Protostars and Planets IV, ed. V. Mannings, A. P. Boss, & S. S. Russell (Tucson, AZ: Univ. Arizona Press), 299
MacDonald, G. H., Gibb, A. G., Habing, R. J., & Millar, T. J. 1996, A&AS, 119, 333
McMullin, J. P., Waters, B., Schiebel, D., Young, W., & Golap, K. 2007, in ASP Conf. Ser. 376, Astronomical Data Analysis Software and Systems XVI, ed. R. A. Shaw, F. Hill, & D. J. Bell (San Francisco, CA: ASP), 127
Meixner, M., Panuzzo, P., Roman-Duval, J., et al. 2013, AJ, 146, 62
Müller, H. S. P., Schlöder, F., Stutzki, J., & Winnewisser, G. 2005, JMoSt, 742, 215
Müller, H. S. P., Thorwirth, S., Roth, D. A., & Winnewisser, G. 2001, A&A, 370, L49
Nomura, H., & Millar, T. J. 2004, A&A, 414, 409
Oliveira, J. M., van Loon, J. T., Sloan, G. C., et al. 2013, MNRAS, 428, 3001
Ossenkopf, V., & Henning, T. 1994, A&A, 291, 943
Pickett, H. M., Poynter, R. L., Cohen, E. A., et al. 1998, J. Quant. Spec. Radiat. Transf., 60, 883
Qin, S.-L., Wu, Y., Huang, M., et al. 2010, ApJ, 711, 399
Sewiło, M., Cordiner, M., Charnley, S. B., et al. 2022a, ApJ, 931, 102

Sewiło, M., Indebetouw, R., Charnley, S. B., et al. 2018, ApJL, 853, L19
Sewiło, M., Karska, A., Kristensen, L. E., et al. 2022b, ApJ, 933, 64
Shimonishi, T., Dartois, E., Onaka, T., & Boulanger, F. 2016a, A&A, 585, A107
Shimonishi, T., Das, A., Sakai, N., et al. 2020, ApJ, 891, 164
Shimonishi, T., Izumi, N., Furuya, K., & Yasui, C. 2021, ApJ, 922, 206
Shimonishi, T., Onaka, T., Kawamura, A., & Aikawa, Y. 2016b, ApJ, 827, 72
Shimonishi, T., Watanabe, Y., Nishimura, Y., et al. 2018, ApJ, 862, 102
Shingledecker, C. N., Lamberts, T., Laas, J. C., et al. 2020, ApJ, 888, 52
Sutton, E. C., Peng, R., Danchi, W. C., et al. 1995, ApJS, 97, 455
Tokuda, K., Zahorecz, S., Kunitoshi, Y., et al. 2022, ApJL, 936, L6
van der Tak, F. F. S., van Dishoeck, E. F., & Caselli, P. 2000, A&A, 361, 327

van Loon, J. T., Oliveira, J. M., Gordon, K. D., Sloan, G. C., & Engelbracht, C. W. 2010, AJ, 139, 1553
Vidal, T. H. G., & Wakelam, V. 2018, MNRAS, 474, 5575
Wang, M., Chin, Y.-N., Henkel, C., Whiteoak, J. B., & Cunningham, M. 2009, ApJ, 690, 580
Ward, J. L., Oliveira, J. M., van Loon, J. T., & Sewiło, M. 2017, MNRAS, 464, 1512
Watanabe, N., & Kouchi, A. 2002, ApJL, 571, L173
Whittet, D. C. B., Cook, A. M., Herbst, E., Chiar, J. E., & Shenoy, S. S. 2011, ApJ, 742, 28
Wilson, T. L., & Rood, R. 1994, ARA&A, 32, 191
Xu, J.-L., & Wang, J.-J. 2013, MNRAS, 431, 2385
Zernickel, A., Schilke, P., Schmiedeke, A., et al. 2012, A&A, 546, A87